CHALMERS
UNIVERSITY OF TECHNOLOGY

Numerical methods for mapping band-type resonance in insect flight

Congxiao Zhang

DEPARTMENT OF MATHEMATICAL SCIENCES

CHALMERS UNIVERSITY OF TECHNOLOGY

Gothenburg, Sweden 2024
www.chalmers.se

MASTER'S THESIS 2024

Numerical methods for mapping band-type resonance in insect flight

Congxiao Zhang

CHALMERS
UNIVERSITY OF TECHNOLOGY

Department of Mathematical Sciences
CHALMERS UNIVERSITY OF TECHNOLOGY

Gothenburg, Sweden 2024

Numerical methods for mapping band-type resonance in insect flight

Congxiao Zhang

Supervisor: Arion Pons, Department of Mechanics and Maritime Sciences, Chalmers, Sweden
Examiner: Larisa Beilina, Department of Mathematical Sciences, Chalmers/GU, Sweden

Master's Thesis 2024

Chalmers University of Technology

SE-412 96 Göteborg
Telephone +46 31 772 1000

Gothenburg, Sweden 2024

Numerical methods for mapping band-type resonance in insect flight
Congxiao Zhang
Department of Mathematical Sciences
Chalmers University of Technology

Abstract

Insect flight is a highly complex and energy-intensive process. Flapping-wing insects employ a unique muscle contraction mechanism that enables high-frequency wing beats, with metabolic rates reaching several times those at rest. Their remarkable endurance during flight highlights the importance of understanding the energy optimization involved. This thesis focuses on developing numerical methods to map band-type resonance, which serves as a benchmark for assessing whether a system achieves an energy-optimal state. We describe the mapping of band-type resonance as an optimization problem and propose two primary numerical methods: particle swarm optimization and numerical continuation. We evaluate the accuracy of the numerical solutions via the solution work loops and power waveforms and compare them with analytical approximations to the space of band-type resonant states. Our findings reveal that while the standalone particle swarm method can provide a relatively complete set of estimated solutions, the solution space lacks continuity. The numerical continuation method sacrifices some completeness in finding solution sets to ensure better continuity in the corresponding domain of the output solution set.

After comparing these methods' performance in identifying potential solutions for simple cases, we improve them and propose a compound numerical method for solving more complex problems, such as higher harmonic and nonlinear oscillators. Notably, this compound algorithm performs well not only on simple linear cases with known analytical solutions but also on complex problems lacking analytical solutions, offering a valuable numerical tool for estimating the mapping zone of band-type resonance when analytical methods are not feasible.

Comparing the results of mapping zones of band-type resonance with wingbeat frequency modulation behaviour observed in actual insect species suggests that such behaviour may be consistent with sustained resonant energy savings by exploiting band-type resonance.

This report is written in English.

Keywords: insect flight motor, energy efficiency, band-type resonance, particle swarm optimization, numerical continuation, work loop

Acknowledgements

I would like to express my heartfelt gratitude to my supervisor, Arion Pons, for his invaluable guidance, unwavering support, andprofound insights throughout the journey of this master's thesis. His expertise and encouragement have shaped both this research and my academic growth.

A special thanks goes to my parents, whose unconditional love, patience, and support have been my pillars of strength throughout my

academic pursuits. Their belief in me has been a constant source of motivation, especially during challenging times.

I am also grateful to the faculty members at the university for creating a stimulating academic environment that fosters critical thinking and innovation.

Lastly, I extend my appreciation to all those who have contributed, directly or indirectly, to the completion of this thesis. Your support has been crucial in bringing this work to fruition.

Congxiao Zhang, Gothenburg, Nov 2024

Contents

Chapter 1

Introduction

1.1 Background

Insects have long fascinated researchers, not only due to their species diversity but also because of their extraordinary flight capabilities. Early research in the 1970s introduced the complex three-dimensional motions of insect wings during flapping [33, 32, 34]. After that, more detailed investigations revealed that, in a process that varies significantly between species, sets of muscles and exoskeletal mechanisms interact to generate finely tuned wingbeat oscillation and, thus, propulsive forces. This discovery helped explain how insects can generate sufficient lift despite their small wing size. To comprehend and analyse the intricate aerodynamics and control systems involved in insect flight mechanisms, researchers employ a variety of dynamic models. These include Computational Fluid Dynamics (CFD) models, which simulate airflow around flapping insect wings to reveal complex phenomena; quasi-steady blade element models, which estimate forces and moments produced by wings based on experimental measurements from dynamically scaled robotic models; and integrated models, which combine multiple components to simulate complete flight behavior [5] *etc*. These sophisticated models enable researchers to investigate aspects of insect flight that are challenging to measure experimentally, such as open-loop dynamics and the effects of specific control strategies [38]. The development of these models has been significantly advanced by recent progress in high-speed videography, computational power, and experimental techniques like digital particle image velocimetry (DPIV)[30]. Inspired by the remarkable efficiency and performance of flying insects in terms of flight range, endurance, and maneuverabilitywith single flights lasting hours to days and covering tens to thousands of kilometres [21, 13], as well as complete body re-orientations on millisecond timescalesresearchers have developed robotic flappers to study insect flight mechanisms and create bio-inspired designs.

This advanced the development of flapping-wing micro-air vehicles (FW-MAVs), which aim to replicate the extraordinary capabilities of insect flight, potentially revolutionising fields such as aerial robotics and environmental monitoring[36, 2, 23, 20].

1.2 Resonance

Many insect species are thought to have developed spring-like elements within their thoraxes and muscles, which help reduce the energetic demands of flapping flight by storing and releasing wingbeat kinetic energy —leading to flight power reductions of up to 30% in certain species and conditions [29, 11, 31]. This "thorax-wing" system can enable resonance, where the elastic components of the insect's bodywork are in harmony with the wing movements to optimise the energy cost. Previous work in the study of resonance in insect flight introduced the concept of dynamic efficiency in flapping flight [7, 8] helping quantify how effectively insects convert metabolic energy into useful aerodynamic work, providing insights into the energy economy of insects and flapping-wing mechanisms. To better understand the interplay between elasticity, damping, and aerodynamics, researchers have developed spring-wing models and conducted experiments using dynamically scaled biophysical flapping models. This helped elucidate more details on how insects utilise frequency and asymmetry modulation for precise flight control.

Insects with synchronous flight muscles directly control wing oscillations through neuronal output, while those with asynchronous muscles, such as beetles, use neuronal signals to turn flight on and off and adjust wing beat frequency for power modulation [18, 19], which may serve as inspiration for the design of insect-scale vehicles with flapping wings[24]. However, in reality, controlling flight through modulation of waveform asymmetry or drive frequency typically results in system efficiency loss. Resonance in insect flight motors is not a unitary state at a single frequency but rather a complex cluster of distinct and mutually exclusive states, each representing a different form of resonant optimality [26]. This complex resonance characteristic allows insects to maintain near-perfect resonant energetic optimality over significant ranges of wingbeat frequencies [26]. To reveal how insects can operate efficiently across a range of frequencies rather than being constrained to a single resonant frequency, it is important to measure the band-type resonance of insects to determine whether they flap at resonance to maximise efficiency or flap off-resonance, sacrificing efficiency for control [12]. Band-type resonance also provides a framework for comprehending how insects balance the conflicting demands of energetic efficiency and flight control, offering insights into insect flight motors' extraordinary robustness and adaptability.[24] This is essential for understanding the trade-offs between energy efficiency and wing manoeuvrability in insect flight[22].

One phenomenon that sheds light on related questions is that of band-type resonance: the ability of both linear and nonlinear forced oscillators to achieve resonant levels of energy efficiency not only at their discrete simple-harmonic resonant states but within a continuous band of fundamental frequencies around these states [28]. This invariant efficiency is achieved via a spectral shaping process, in which the input forcing waveforms are tuned away from simple harmonicity to ensure that power flows only from the forcing actuator to the oscillator and never in reverse—an unidirectional flow of power matching that of a simple-harmonic resonant state [28, 27]. Band-type resonance could enable insect and insect-inspired propulsion systems to achieve specific wingbeat control modulations without loss of efficiency and without varying the propulsion system's structural properties, but details are unclear. In particular, mapping the zone of band-type resonant states is a difficult task, even in linear oscillators, because it is difficult to establish the exact level of frequency modulation. Analytical and parametric approximations, as used previously [28, 27], provide only conservative bounds on the size of the resonant band in linear cases. Therefore, in order to map the entire region of band-type resonance and investigate this type of issue in more broad scenarios, numerical methods are needed.

1.3 Outline of the thesis

In this thesis, we develop novel numerical methods for mapping the zone of band-type resonant states in general single-degree-of-freedom (1DOF) oscillators, based on numerical continuation and particle-swarm optimisation in combination with a local iterative optimisation algorithm. We, firstly, apply these methods to map the zone of band-type resonant states in 1DOF linear models of an insect flight motor—focusing, in particular, on the band of states across wingbeat fundamental frequency, *i.e.*, frequency-band resonance [28]. In Chapter 2, we propose a dynamic model of the wing oscillation of a general insect, based on a 1DOF parallel-elastic actuation (PEA) system. In Chapter 3, we formulate the problem of mapping band-type resonance as an optimisation problem and present the basic principles of the particle swarm method and numerical continuation method; and in Chapter 4, we show the results of these two methods used on the 1DOF PEA system and analyse their performance. Chapter 5 presents an improved optimisation algorithm applied to more complicated cases, including mapping spaces with much higher harmonics and nonlinear oscillators. Finally, Chapter 6 provides a concluding summary. Related Code can be found in [37].

Our mapping results, in combination with observations of wingbeat frequency modulation behaviour in insects and proposed frequency modulation control strategies in FW-MAVs, indicate that band-type resonance may be a feasible strategy for wing-

beat frequency modulation and that the available modulation amplitude is larger than previously thought —sufficiently large to, in theory, account for many behaviours observed in insects. The numerical method presented in the thesis also provides a valuable tool for biologists and engineers studying insect flight, designing MAVs, etc. This can also effectively help researchers to improve the efficiency, agility, and flight capability of MAVs.

Chapter 2

Dynamic modelling of the insect flight motor

Insect flight muscles generate resonant oscillations of the thorax[17]. These muscles are categorised as direct flight muscles, which attach to the wings; and indirect flight muscles, which deform the thorax to move the wings[15]. The indirect flight muscles consist of two antagonistic sets: dorso-longitudinal muscles (DLM) and dorso-ventral muscles (DVM)[4]. During wings takeoff, the DVM contracts and deforms the thorax, causing the DLM to extend and undergo delayed stretch activation. This delayed force generation by the DLM leads to the contraction and the extension of the DVM[4]. This process establishes a cycle of stretching and contracting, resulting in repeated thoracic oscillations for each nerve impulse and enabling efficient high-frequency flight [3]. Fig.2.1(a)[4] shows an example with details in alternating contraction indirect insect flight muscles that cause flapping wing movements. A more straightforward illustration of this biological process is given as Fig.2.1(b) [26], which depicts the indirect flight muscles with a 1DOF PEA oscillator and the whole thorax-wing system as a hybrid dynamic model. Generally, a 1DOF PEA system [28] is formulated by ordinary differential equations comprising inertial, elastic, damping, and actuator load terms. The system can be expressed in both general and canonical forms:

	inertial		damping		elastic		actuator load
General Form:	$m\ddot{x}$	+	$d\dot{x}$	+	kx	=	F
Canonical Form:	$\ddot{x}$	+	$2\xi\omega_0\dot{x}$	+	$\omega_0^2 x$	=	f

In these equations, $x = x(\omega, t)$ represents the displacement (e.g., of thorax or wings), ξ is the damping ratio, and ω_0 denotes the natural frequency [16, 35]. The output power

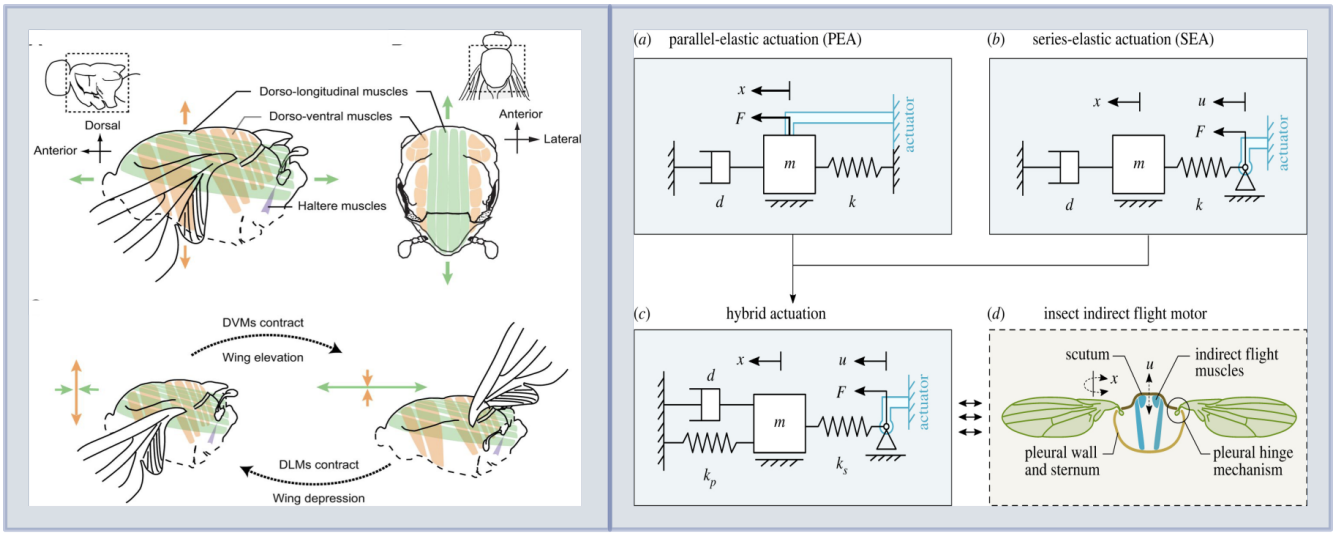

(a) (b)

Figure 2.1: (a) An illustration of biological mechanics structures of insect wings: The structure of the indirect flight muscles is shown in the upper part of the figure. The bottom part depicts the resonant contraction cycle and extension of the muscles and wings movements; (b) A hybrid 1DOF model of an indirect flight motor. The mechanics model of the 1DOF PEA system is also presented.

of the actuator in this system is defined as

$$p = f(\xi, x(\omega, t))\dot{x}(\omega, t) = p(\xi, \omega, t) \tag{2.1}$$

Band-type resonance is characterised by a frequency space Ω[28] defined as,

$$\Omega = \{\omega | p(\xi, \omega, t) \geq 0, \forall t \in \mathbb{T}\} \tag{2.2}$$

where $\mathbb{T}$ denotes the entire time domain, ω_0 is the natural frequency and the solution set $\mathbb{S}$ is denoted as,

$$\mathbb{S} = \{(\xi, \omega/\omega_0) | p(\xi, \omega, t) \geq 0, \forall t \in \mathbb{T}\}. \tag{2.3}$$

The solutions given above fulfill the demands to achieve the optimal absolute mechanical power consumption and system efficiency. It minimises energy dissipation by ensuring consistent positive power output throughout the cycle, eliminating periods of negative power[27, 4]. The solution set $\mathbb{S}$ includes both the conventional energy-resonant state (producing simple-harmonic motion) and frequency-band resonant states (outputting multi-harmonic waveforms with fundamental frequencies away from the energy-resonant frequency). Determining this solution set is challenging, as it requires searching all possible periodic waveforms over a given fundamental frequency window. Currently, there are no estimates of the full set, even for linear systems, nor definitive evidence that the complete set of frequency-band states forms a single frequency interval. Numerical approaches to mapping these frequency band

states can address these knowledge gaps[27, 25].
In order to properly represent the band-type resonance in the system, we must first determine how to express the displacement for specific circumstances. In general cases, a periodic function $x(t)$ representing the system's response can be expressed as a Fourier series:

$$x^i(t) = a_0^i + \sum \left[a_k^i \cos\left(k\omega_i t\right) + b_k^i \sin\left(k\omega_i t\right)\right] \tag{2.4}$$

where $k = 1, 2, 3, \cdots$, ω is the fundamental frequency, a_k and b_k are the Fourier coefficients, i means the i-th element in the corresponding vector space, for example, a_k^i means the k-th element in the i-th vector $\mathbf{A}^i$ in the Fourier odd harmonic coefficient space$\mathbb{A}$. To simplify the problem, we assume $x^i(t)$ consists only of odd harmonics, resulting in a cosine-only series:

$$x^i(t) = \sum_{k=1}^{n} [a_k^i \cos\left(k\omega_i t\right)] \tag{2.5}$$

This formulation ensures that $x^i(t)$ is even-symmetric about the nominal stroke extrema. However, this simplification process may limit the accuracy of approximating non-smooth waveforms. When considering multiple waves $x^i(t)$ at different fundamental frequencies ω_i, we observe that any wave can be reconstructed at certain lower nominal fundamental frequencies by setting lower-frequency amplitudes to zero and using higher harmonics to alias back onto the original wave. This phenomenon can lead to different mapping sub-zones representing the same solutions. To prevent this aliasing effect and ensure that the fundamental frequency ω_i accurately represents the dominant period of the wingbeat, we must constrain its amplitude coefficient vector: $\mathbf{A}^i = [a_1^i, a_2^i, \cdots, a_k^i, \cdots, a_n^i]$ during problem formulation by $|a_1^i| \geq 0.5$.
In this context, we seek solutions $\{(\xi_i, \omega_i) | i \in \{1, 2, \cdots, N\}\}$ that satisfy:

$$p_{\xi_i}(\omega_i, t) = p(\xi_i, \omega_i, t) \geq 0, \ \forall t, \tag{2.6}$$

where $\mathbf{A}^i = [a_1^i, \cdots, a_m^i]$, the coefficients of the related displacement $x^i(t)$ are also unknown. Using the waveform parameterization from the Eq. 2.5-2.6, we can directly evaluate the derivatives $\dot{x}$ and $\ddot{x}$, , and consequently the functional $p_\xi(\omega, t)$ can be evaluated directly at any pair of frequency and time points (ω, t) via the associated Fourier series.
Our aim is to identify key characteristics within the solution space $\mathbb{S}$ (see Eq. 2.3), such as the continuity, extreme points, and boundaries. In this thesis, a 1DOF PEA linear and a nonlinear system are being considered:

$$\begin{aligned} &\text{1DOF PEA system (linear):} && \ddot{x}(t) + 2\xi\dot{x}(t) + \omega_0^2 x(t) = f, \\ &\text{nonlinear system:} && \ddot{x}(t) + 2\xi|\dot{x}(t)|\dot{x}(t) + \omega_0^2 x(t) = f, \end{aligned} \tag{2.7}$$

Chapter 3

Numerical methods for mapping band-type resonance

3.1 Formulation as a discrete optimization problem:

We begin by developing a discretisation framework based on the original problem (Eq.2.7). This discretisation involves three steps:

1. Using an Operator $\mathcal{Q}$ we define the matrix operation $\dot{\mathbf{x}} = \mathcal{Q}\mathbf{x}$, where $\mathbf{x}, \dot{\mathbf{x}} \in \mathbb{R}^n$ is the discrete-time representation of x and $\dot{x}$. $\mathcal{Q} \in \mathbb{R}^{n \times n}$ is defined as

$$\mathcal{Q} = \begin{bmatrix} 1 & 0 & 0 & 0 & \cdots & 0 & 0 \\ -1 & 1 & 0 & 0 & \cdots & 0 & 0 \\ 0 & -1 & 1 & 0 & \cdots & 0 & 0 \\ \vdots & \vdots & \vdots & \vdots & \ddots & \vdots & \vdots \\ 0 & 0 & 0 & 0 & \cdots & -1 & 1 \end{bmatrix} \frac{1}{\Delta t}, \tag{3.1}$$

   and so $\mathcal{Q}\mathbf{x}$ is the discrete-time derivative of x based on the forward difference method, where $\mathbf{x}$ is obtained by assuming that there are $(n-2)$ *anchor points* cutting the time domain of $t \in [0, 2\pi/\omega]$ into n intervals. x_k is the kth element of the displacement vector $\mathbf{x} = [x_1, x_2, \cdots, x_k, \cdots, x_n]$, *i.e.*, the anchor points. The related interpolated time sequence $\mathbf{t}$ is defined as $\mathbf{t} = [t_1, t_2, \cdots, t_m], \Delta t = t_k - t_{(k-1)}$ is a constant, *i.e.*, the grids has equidistant-distant grids.

2. Then the equations of motion can be approximated as:

$$\begin{aligned}\mathbf{f} &= \mathcal{Q}\mathcal{Q}\mathbf{x} + 2\omega_0\mathcal{Q}\mathbf{x} + \omega_0^2\mathbf{x} \\ &= (\mathcal{Q}^2 + 2\omega_0\mathcal{Q} + \omega_0^2)\mathbf{x} \\ &= \mathcal{A}\mathbf{x},\end{aligned} \tag{3.2}$$

where $\mathcal{A} = \mathcal{Q}^2 + 2\omega_0\mathcal{Q} + \omega_0^2 \in \mathbb{R}^{N\times N}$ is the operator stiffness matrix; $\mathcal{Q}^2 \in \mathbb{R}^{N\times N}$ is the matrix that computes the second order derivative; and $\mathbf{f}, \ddot{\mathbf{x}}, \dot{\mathbf{x}}, \mathbf{x} \in \mathbb{R}$ are the discrete-time versions of, for example, the muscle force, wing stroke angular acceleration, wing stoke angular velocity or wing stroke angle.

3. Finally, the discrete estimate of muscle or actuator instantaneous power consumption, $\mathbf{p}$, is:

$$\begin{aligned}\mathbf{p} &= \mathbf{f}\dot{\mathbf{x}} = \mathcal{B}\mathbf{x} \\ \mathcal{B} &= \mathcal{A}\mathcal{Q}.\end{aligned} \tag{3.3}$$

Consider then the problem of solving for a band-type resonant state at a given frequency $\omega = \omega_i$, in the vicinity of some initial guess of waveform coefficients, $\mathbf{A}^0 = [a_1^0, a_2^0, \cdots, a_m^0]$.
Rewriting the formula of $x(t)$ (Eq.2.5) into discrete matrix form, we have:

$$\begin{aligned}\mathbf{x}^i &= \mathbf{A}^i\mathbf{H}^i \\ \mathbf{A}^i &= [a_1^i, a_2^i, \cdots, a_k^i, \cdots, a_m^i] \\ \mathbf{H}^i &= [\cos(\omega_i\mathbf{t}), \cos(2\omega_i\mathbf{t}), \cdots, \cos(k\omega_i\mathbf{t}), \cdots, \cos(m\omega_i\mathbf{t})]^{\mathrm{T}}\end{aligned} \tag{3.4}$$

where $\mathbf{H}^i$ denote the i-th suffix-harmonic matrix. The trigonometric form of elements in the suffix-harmonic matrix gives a convenient way to replace a tedious decomposition process with a series of simpler steps. For the derivatives of $\mathbf{x}$:

$$\begin{aligned}\ddot{\mathbf{x}}^i &= \mathbf{A}^i\ddot{\mathbf{H}}^i \\ \dot{\mathbf{x}}^i &= \mathbf{A}^i\dot{\mathbf{H}}^i \\ \mathbf{A}^i &= [a_1^i, a_2^i, \cdots, a_k^i, \cdots, a_m^i] \\ \ddot{\mathbf{H}}^i &= -[\omega_i^2\cos(\omega_i\mathbf{t}), 4\omega_i^2\cos(2\omega_i\mathbf{t}), \cdots, k^2\omega_i^2\cos(k\omega_i\mathbf{t}), \cdots, m^2\omega_i^2\cos(m\omega_i\mathbf{t})]^{\mathrm{T}} \\ \dot{\mathbf{H}}^i &= -[\omega_i\sin(\omega_i\mathbf{t}), 2\omega_i\sin(2\omega_i\mathbf{t}), \cdots, k\omega_i\sin(k\omega_i\mathbf{t}), \cdots, m\omega_i\sin(m\omega_i\mathbf{t})]^{\mathrm{T}}.\end{aligned} \tag{3.5}$$

Our goal is to determine the frequency band, in the whole frequency domain Ω, that satisfies the non-negative condition of power, $\mathbf{p}^i \geq 0$, for non-trivial $\mathbf{x}^i$ [27]. To achieve the optimisation object and improve the efficiency and accuracy of the optimisation algorithm, we compute $\min\mathbf{p}^i$ and $\max\mathbf{p}^i$, as well as $\min\mathbf{x}^i$ and $\max\mathbf{x}^i$, and use them to define up a power ratio metric η^i [26] and an x-amplitude metric r^i to normalise the

optimisation parameters:

$$\eta^i = -\frac{\min \mathbf{p}^i}{\max \mathbf{p}^i}, \quad r^i = \max \mathbf{x}^i - \min \mathbf{x}^i, \tag{3.6}$$

where these metrics are now numerically-computable functions of $\mathbf{A}^i$. We then seek $\mathbf{A}^i$ such that η^i is minimised, subject to the constraints that $r^i = 2$ (normalized amplitude) and $\left(a_1^i\right)^2 \geq 1/4$ (prominent fundamental frequency). We choose this specific objective($\min \eta^i$) to make sure the algorithm is sensitive enough to changes in the value of the minimum of $\mathbf{p}^i$. Dividing the minimum of $\mathbf{p}^i$ by the maximum of $\mathbf{p}^i$ will not give η^i a different sign from the minimum of $\mathbf{p}^i$ because the maximum of $\mathbf{p}^i$ will always be positive. To achieve the objective, the algorithm will try to find those $\min \mathbf{p}^i \geq 0$, or, if $\min \mathbf{p}^i \geq 0$ can not be achieved, the algorithm will try to find those $\min |\mathbf{p}^i|$ that is sufficiently close to 0 in certain situation. The constraint on r^i is a normalisation constraint which eliminates duplicated solutions, *e.g.*, $\mathbf{A}^{'} = c\mathbf{A}^0$, where c is a constant. The constraint on $\left(a_i^1\right)^2$ is to make sure the solution waveform will always be dominated by its fundamental frequency. Then, the general optimisation model can be summarised as follows:

$$\begin{aligned}
&\textbf{variables:} && \mathbf{A}^i = [a_1^i, a_2^i, \cdots, a_k^i, \cdots, a_m^i] \\
&\textbf{minimize:} && \eta_i \\
&\textbf{subject to:} && r_i = 2 \\
& && \left(a_1^i\right)^2 \geq 1/4.
\end{aligned}$$

3.2 Solution via particle swarm optimization

The particle swarm methods follows exactly the optimisation procedure with specific initialization process and two optimisation solvers, scanning the potential solutions on a selected window on the $\xi - \omega/\omega_0$ Space. By set up several particles randomly as the initialisations in the search space, each representing a potential solution, particle swarm optimization method will iteratively improve potential solutions with respect to a given measure of quality[10]. During this process, the fitness of each particle is evaluated according to the predefined objective function (given as the optimization objective function in Section 3.1)[9]. For each category, the input damping ratio ξ range from 0 to 1, denoted as $\xi \in [0, 1]$ and omega ratio ω/ω_0 range from 0 to 2, denoted as $\omega/\omega_0 \in [0, 2]$. The choice of this interval is based on the following considerations:

- **Damping ratio ξ selection**: When the damping ratio ξ exceeds one, that $\xi > 1$,

the system becomes overdamped. In an overdamped system, the return to equilibrium is slow and lacks oscillatory behaviour, which contrasts sharply with the natural dynamics of insect flight, where rapid and efficient oscillatory motions are essential for manoeuvrability and stability. Therefore, restricting ξ to a maximum of 1,that $\xi \leq 1$ ensures the simulation remains representative of real-world insect flight conditions, which typically involve underdamped or critically damped systems for optimal performance.

- **Frequency ratio ω/ω_0 selection**: The range of the frequency ratio ω/ω_0 is derived from extensive simulation data. Various ranges were tested to determine the most appropriate upper bound. The analysis consistently showed that the extreme values of ω/ω_0 did not exceed 2, that $\omega/\omega_0 \leq 2$, within the solution set. Hence, selecting 2 as the upper limit ensures a comprehensive yet practical range for the simulations, capturing all relevant resonant behaviors without unnecessary computational overhead.

We experimented with two approaches for assigning initial values to the vector $\mathbf{A}$.

- Fixed Initialization of $\mathbf{A^0}$: In this approach, the optimization algorithm consistently uses the same initial values for $\mathbf{A^0}$, *e.g.*, for a 3-term case $\mathbf{A^0} = [0.5, 0.5, 0.5]$. These values are arbitrary and chosen primarily to ensure the optimization solver runs correctly. Although the initialisation value is fixed, this initialisation process provides a baseline for assessing the algorithm performance and stability under consistent starting conditions.
- Gaussian Sampling Initialization: To introduce variability and test the stability of the particle swarm method, we generated s samples using the gaussian sampling method within the vector space $[-1, 1]^m$, where m denotes the term number of case, *e.g.*, for a 3-term case $[-1, 1]^m = [-1, 1]^3$.

Two distinct solvers are employed to find solutions to the remaining local optimization problem:

- **The Active-set method**: This algorithm is well-suited for solving constrained problems and operates by maintaining a working set of inequality constraints by transforming the whole problem into a set of simple equality-constrained subproblems. It is particularly useful when the number of constraints is larger than the number of variables, as it reduces the problem's complexity.
- **Sequential Quadratic Programming (SQP)**: SQP is a powerful optimisation technique that solves a sequence of quadratic programming sub-problems, converging to a solution that satisfies both the objective function and constraints[6].

Compared to the Active-set Method, SQP is a broader method that often incorporates Active-set methods as a component, because many SQP implementations use active-set strategies to solve the quadratic programming sub-problems at each iteration [14]. While active-set methods are efficient for problems with many constraints relative to variables, SQP is particularly effective for highly nonlinear problems[14]. As a summary, we are giving the pseudo-code to depict the whole workflow (See Algorithm 1, Algorithm 2).

Algorithm 1 Workflow: Particle swarm Algorithm (Fixed Initialization)

Require: Initialization of parameters: Damping Ratio ξ, Natural Frequency ω_0
  for Damping Ratio $\xi \rightarrow$ Defined Domain [0,$\cdots$] **do**
    while Omega Ratio $\Theta = \omega/\omega_0 \rightarrow$ Defined Domain [1,$\cdots$] **do**
      Initialization: Fixed Initialization $\mathbf{A^0} = [0.1, 0.1, 0.1, \cdots]$;
      Optimization Solver (**SQP or Active Set**);
      Check the solution given by the solver
      if Solution α^* fulfil the tolerance **then**
        Output the solution;
      end if
      Update Omega Ratio with step width h:
      $\Theta_{\text{NEW}} = (\omega/\omega_0)_{\text{NEW}} = \Theta_{\text{OLD}} + h = (\omega/\omega_0)_{\text{Old}} + h$
    end while
  end for

3.3 Solution via numerical continuation

Numerical continuation is a class of computational techniques used to analyze the behavior of nonlinear systems by tracking the solutions of these systems as a parameter within the system varies. These methods are particularly valuable in biomechanics and biomimetics, where systems often exhibit complex nonlinear behaviors due to the intricacy of biological tissues and structures. Within nonlinear dynamics, numerical continuation methods are standard tools for analyzing nonlinear differential equations. Fundamental principles and methods, such as the predictor-corrector (PC) method and the pseudo-arclength (PL) method (See Fig.3.1), are presented in [1].
Classical numerical continuation method is to obtain a solution to a system of N nonlinear equations in N variables [1], say:

$$\mathbf{F}(x) = 0 \tag{3.7}$$

where common iterative numerical methods, *e.g.*, Newton-type algorithms, will always fail due to the pre-claimed situations. The idea in the PC method is to numerically

Algorithm 2 Workflow: Particle swarm Algorithm (Gaussian Sampling)

Require: Initialization of parameters: Damping Ratio ξ, Natural Frequency ω_0
  for Damping Ratio $\xi \rightarrow$ Defined Domain [0,$\cdots$] **do**
    while Omega Ratio $\Theta = \omega/\omega_0 \rightarrow$ Defined Domain [1,$\cdots$] **do**
      Initialization: Gaussian Sampling $\mathbf{A^0} = \beta^j$, β^j is j-th element in the Sample Set, $j = 1$ in the intialisation step;
      Optimization Solver (**SQP or Active Set**);
      Check the solution given by the solver
      if Solution α^* fulfil the tolerance **then**
        Output the solution;
      else if Solution α^* doesn't fulfil the tolerance **then**
        j = j+1 (*!!Entrance of Gaussian Sampling!!*)
        $\mathbf{A^0} = \beta^j$, β^j is j-th element in the Sample Set;
        Optimization Solver;
        Check the solution given by the solver;
        if Solution α^* fulfil the tolerance **then**
          Output the solution;
          Go to the 'Exit' Step
        else if Solution α^* doesn't fulfil the tolerance **then**
          Turn back to the 'Entrance of Gaussian Sampling' step
        end if
      end if(*!!Exit!!*)
      Update Omega Ratio (ω/ω_0) with step width h:
      $\Theta_{\text{NEW}} = (\omega/\omega_0)_{\text{NEW}} = \Theta_{\text{OLD}} + h = (\omega/\omega_0)_{\text{Old}} + h$
    end while
  end for

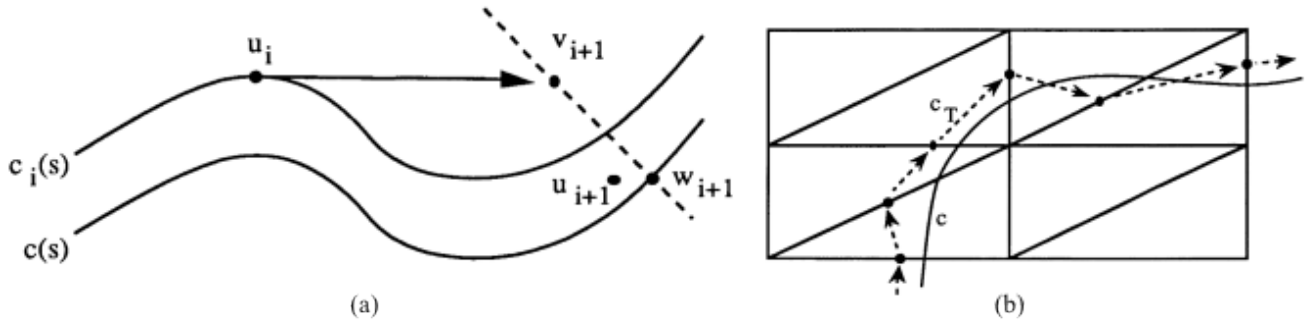

Figure 3.1: An illustration of traditional numerical continuation methods [1]. (**a**): PC path following; (**b**): PL path following.[1]

trace the analytical solution curve c by generating a sequence of points $u_i, i = 1, 2, \cdots$ along the curve satisfying a chosen tolerance criterion, where $c_i(s)$ represents the approximate solution curve corresponding to each u_i. To obtain a new approximate solution as close as possible to the analytical solution curve c (which assures the approximation is accurate enough), a predictor step is defined via an Euler process[14].

Let w_{i+1} denote the analytical solution for the next iteration on the analytical solution curve c, v_{i+1} denotes the 'guess' solution given by the predictor step; refer to the approximate solution u_i in the last step. If u_i is sufficiently close to the analytical solution curve c and the stepsize is sufficiently small, then the predictor point v_{i+1} which denotes the 'corrector' result given by the first 'corrector' iteration using the approximate solution u_i as an initialisation will be sufficiently close to the analytical solution curve c, which means that we can finally get an approximation of w_{i+1} after several 'corrector' iterations (*e.g.*, a Newton-like method) with a given tolerance denoted as u_{i+1}. The idea of the PL method is quite similar to the PC method: it follows exactly a piecewise-linear curve c_Γ that approximates the analytical solution curve c. Tracing the path is carried out via PL steps similar to the steps used in linear programming methods, *e.g.*, the simplex method.

The process of mapping band-type resonance does not deal with a problem of exactly this form but will be quite similar in the basic principles. We can assume that the solutions to our optimisation problem form a solution curve over ω, in which case a (broad) numerical continuation method could assist in finding suitable values of $\mathbf{A}^0$, which would make the final mapping zone smoother. In our optimisation algorithm, for any given ξ^*, we can parameterise the function of power p concerning the amplitude coefficients:

$$\Theta = \frac{\omega}{\omega_0}, \qquad \alpha = [a_1, a_2, \ldots, a_m], \tag{3.8}$$

denoted as $p = p(\Theta, \alpha)$. According to the definition of band-type resonance, the trajectory that satisfies our objective function to use is $c_\Theta(\alpha)$, which consists of all Θ^*, α^* that satisfy:

$$\min p(\Theta, \alpha) \geq 0. \tag{3.9}$$

Assume (Θ_1, α_1) and (Θ_2, α_2) are two points on the trajectory $c_\Theta^{\xi^*}(\alpha) = p^{\xi^*}(\Theta, \alpha)$ at $\xi = \xi^*$, with $c_{\Theta_1}^{\xi^*}(\alpha_1) = p(\Theta_1, \alpha_1)$ being known. Similar to the principles of classical continuation methods, we use the power at (Θ_2, α_1) as the 'predictor' for the approximation value of $p^{\xi^*}(\Theta_2, \alpha_2)$, denoted as:

$$\bar{p}^{\xi^*}(\Theta_2, \alpha_2) = p^{\xi^*}(\Theta_2, \alpha_1), \tag{3.10}$$

where $\bar{p}^{\xi^*}(\Theta_2, \alpha_2)$ represent the estimation value of the power function at point (Θ_2, α_2), and use α_1 as the initial value for the optimization variable in the optimization algorithm. The reasons for doing so are as follows:

(Θ_1, α_1) is a known solution which fulfils the constraint that the corresponding minimum of the trajectory $\min c_{\Theta=\Theta_1}^{\xi^*}(\alpha_1) = \min p^{\xi^*}(\Theta_1, \alpha_1) \geq 0$. Suppose Θ_2 is quite near to Θ_1 so that it can be written as $\Theta_2 = \Theta_1 + h$ (where h is a sufficiently small step width). Then we can say:

$$p^{\xi^*}(\Theta_2, \alpha_1) \simeq p^{\xi^*}(\Theta_1, \alpha_1) + h(p^{\xi^*}(\Theta_1, \alpha_1))', \tag{3.11}$$

where $(p^{\xi^*}(\Theta_1, \alpha_1))'$ represents the derivative of $(p^{\xi^*}(\Theta_1, \alpha_1))$ with respect to α_1 at the point (Θ_1, α_1). Thus, we have

$$\min c^{\xi^*}_{\Theta=\Theta_2}(\alpha_1) = \min p^{\xi^*}(\Theta_2, \alpha_1) \simeq \min p^{\xi^*}(\Theta_1, \alpha_1). \tag{3.12}$$

Although $\min c^{\xi^*}_{\Theta=\Theta_2}(\alpha_1) = \min p^{\xi^*}(\Theta_2, \alpha_1)$ is not ensured to be greater than 0, it will at least be 'near' to non-negative. Therefore, when we use (Θ_2, α_1) as the initial value to find the α_2 that fulfils our aim, it will reduce the time cost of the algorithm and also make sure the solution space we found is smooth. Because the solutions given by the

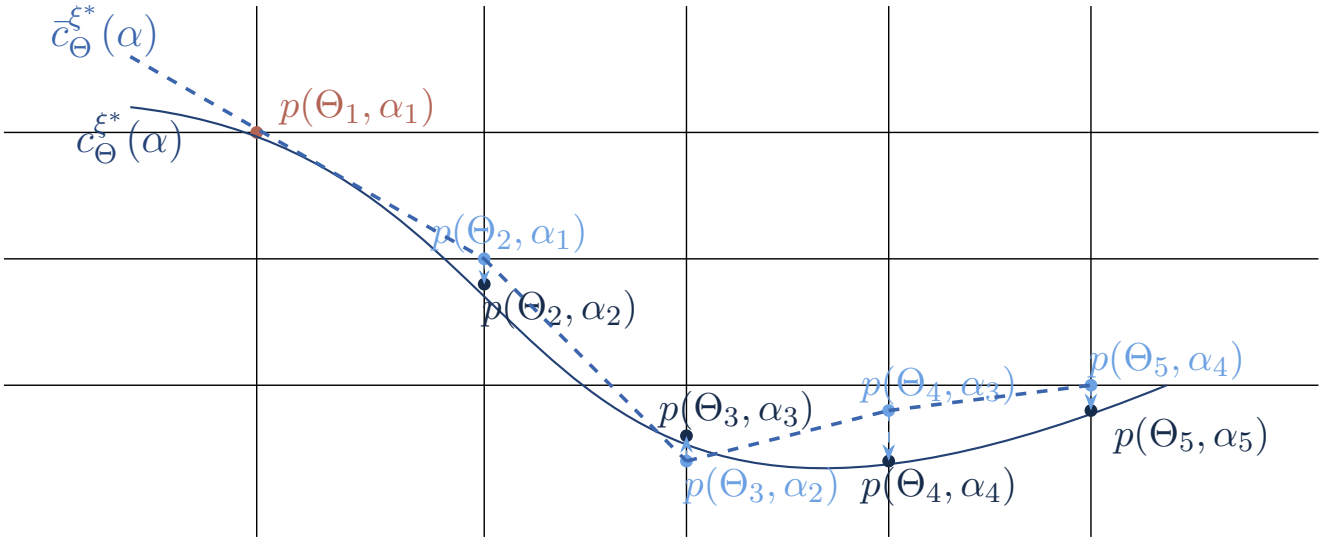

Figure 3.2: An illustration of the process by which we can trace the solution trajectory starting from one known solution $p(\Theta_1, \alpha_1)$. $p(\cdot, \cdot)$ denotes the parameterized power function. The blue nodes (or 'guess' solutions) represent the corresponding power function p to those initial values fed to the optimisation algorithm, and the black nodes represent the final solutions (also parameterised). Then $\bar{c}^{\xi^*}_{\Theta}(\alpha)$ denote the trajectory of 'guess' solutions, and $c^{\xi^*}_{\Theta}(\alpha)$ the trajectory of the solutions given by the optimisation algorithm.

optimisation algorithm are not guaranteed to be non-negative (to within tolerance), we still need a tolerance-check filter step at the end of each numerical continuation step. That is, after we use numerical continuation to find some numerical solutions, we need to check whether they fulfil the constraint that the minimum of the corresponding power function is non-negative. If they fulfil the constraint, we will add the solution to the solution set, and the corresponding trajectory $c^{\xi^*}_{\Theta}(\alpha)$ will continue. If they don't fulfil the constraint, we will break the trajectory $c^{\xi^*}_{\Theta}(\alpha)$ and start a new continuation process with a new known solution $p(\Theta_1, \alpha_1)_{\text{new}}$. In summary, the following

is a pseudo-code describing the complete solution process using numerical continuation. Remember that this numerical continuation process replaces the initialisation process in the particle swarm method.

Algorithm 3 Workflow with numerical continuation method

Require: Initialization of parameters: Damping Ratio ξ, Natural Frequency ω_0
  for Damping Ratio $\xi \rightarrow$ Defined Domain [0,$\cdots$] **do**
    while Omega Ratio $\Theta = \frac{\omega}{\omega_0} \rightarrow$ Defined Domain [1,$\cdots$] **do**
      Initialization: $\alpha = [a_1, 0, \cdots]$;
      Optimization Solver;
      Check the solution given by the solver
      if Solution α^* fulfil the tolerance **then**
        New Initialization for optimization Solver in next iteration: $\alpha = \alpha^*$;
      else if Solution α^* doesn't fulfil the tolerance **then**
        End the current iteration
      end if
      Update Omega Ratio with step width h: $\Theta_{\text{NEW}} = \frac{\omega}{\omega_0\,\text{NEW}} = \Theta_{\text{OLD}} + h = \frac{\omega}{\omega_0\,\text{Old}} + h$
    end while
  end for

Chapter 4

Results for simple mapping tasks

We start the implementation of our algorithm from a simple 3-term odd harmonic oscillator, defined as,

$$x(t) = a_1 \cos(\omega t) + a_2 \cos(3\omega t) + a_3 \cos(5\omega t) \tag{4.1}$$

As presented in Chapter 3, we can discretise these functions as:

$$\begin{aligned}
\mathbf{x}^i &= \mathbf{A}^i \mathbf{H}^i \\
\dot{\mathbf{x}}^i &= \mathbf{A}^i \dot{\mathbf{H}}^i \\
\ddot{\mathbf{x}}^i &= \mathbf{A}^i \ddot{\mathbf{H}}^i \\
\mathbf{A}^i &= [a_1^i, a_2^i, a_3^i] \\
\mathbf{H}^i &= [\cos(\omega_i \mathbf{t}), \cos(3\omega_i \mathbf{t}), \cos(5\omega_i \mathbf{t})] \\
\dot{\mathbf{H}}^i &= [-\omega_i \sin(\omega_i \mathbf{t}), -3\omega_i \sin(3\omega_i \mathbf{t}), -5\omega_i \sin(5\omega_i \mathbf{t})] \\
\ddot{\mathbf{H}}^i &= [-\omega_i^2 \cos(\omega_i \mathbf{t}), -9\omega_i^2 \cos(3\omega_i \mathbf{t}), -25\omega_i^2 \cos(5\omega_i \mathbf{t})]
\end{aligned} \tag{4.2}$$

The subscript i here labels the i-th pair of (ξ, ω). For each pair of (ξ, ω), we choose a time interval of $[t_{\min}, t_{\max}] = [-4\pi/\omega, 4\pi/\omega]$, where the stepsize of the time t is always set up as $\Delta t_i = \frac{T_i}{1000} = \frac{2\pi}{1000\omega_i}$. No matter which initialisation method fixed, gaussian sampling or numerical continuation method) is used, the algorithm will always surf on the $\frac{\omega}{\omega_0} - \xi$ window (ξ range from 0 to 1 and$\frac{\omega}{\omega_0}$ range from 0 to 2) with omega-ratio stepsize $\Delta\frac{\omega}{\omega_0} = 0.01$ and ξ-stepsize $\Delta\xi = 0.01$. The reason is stated in Section. 3.2. The specific optimisation problem associated with this mapping task is:

$$
\begin{aligned}
\textbf{variables:} \quad & \mathbf{A} = [a_1, a_2, a_3] \\
\textbf{minimize:} \quad & \eta^i \\
\textbf{subject to:} \quad & r^i = 2 \\
& \left(a_1^i\right)^2 \geq 1/4
\end{aligned}
$$

We begin with the particle swarm optimisation, with fixed initialization, and initialisation based on Gaussian sampling. For the fixed, initialisation, we choose $\mathbf{A}^0 = [0.1, 0.1, 0.1]$. For initialisation based on the gaussian sampling method, we select two different sample sets by setting (μ, σ) as $(0, 0.5)$ and $(0, 1)$. For each element $a_j \in \mathbf{A}, j = 1, 2, 3$, we assume $a_j^0 \sim N(\mu, \sigma)$. The choice of $\mu = 0$ is based on the symmetrical reference range of a_j (after normalization), which is $[-1, 1]$. This interval is well symmetric about 0, making $\mu = 0$ an appropriate choice.

As per Section 3.3, we need an initial solution set that includes enough initial values as the input of the numerical continuation optimisation algorithm input. It seems to be hard to find such a set; however, considering the specificity of the oscillator, the simple harmonics can naturally fulfil our aim. Thus, the initial solution set, or the 'guess' solution set consists of these elements where $a_1 = 1$ and $a_j = 0, j = 2, 3$. This result has been proved, *e.g.*, in [26]. We benchmarked all these three algorithms with a coarse stepsize ($\Delta\frac{\omega}{\omega_0} = 0.1$ and $\Delta\xi = 0.1$) chosen by running the optimisation algorithm repeatedly 20 times and computing the mean time-cost. The results (time cost for a single iteration) are shown in Table 4.1.

Time (s) Methods / Solvers	**Fixed Initialisation**	**Gaussian Sampling**	**Numerical Continuation Method**
Active-set	33.86	230.15	3.29
SQP	30.82	152.66	6.19

Table 4.1: Benchmark Results of Three different Methods

As per Table 4.1, for particle swarm optimisation, the active-set solver is more expensive than the SQP solver, but for numerical continuation, which seems to be the most efficient method among these three kinds, the result is reversed. The detailed explanation has to consider the results of the band-type resonance mapping zone, so we will introduce it later.

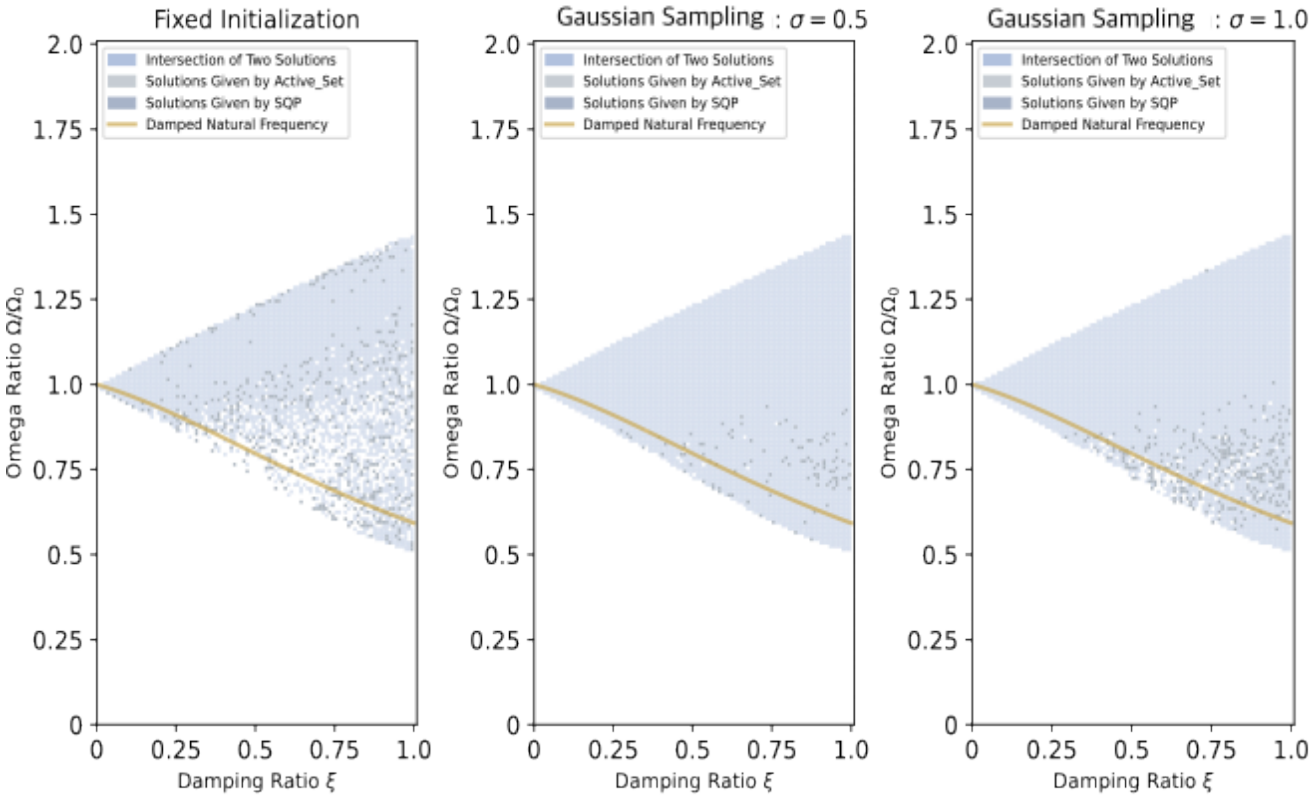

Figure 4.1: Mapping Zone: Fixed Initialization vs. Gaussian Sampling

The mapping zone given by two different initialisation methods of particle swarm algorithm are shown in Fig. 4.1. In sub-figure 1, we utilise the fixed initialization method to initialise the values of amplitude coefficients $\mathbf{A}^k = \{a_1^k, a_2^k, a_3^k\}$. In sub-figure 2, we employ the gaussian sampling method for initialisation. During the generation of initial samples using gaussian sampling for subfigure 2, the standard deviation σ is set to 0.5, whereas for subfigure 3, σ is set to 1. It is evident that the mapping zone obtained using fixed initialization in sub-figure 1 is the worst. Although both sub-figures 2 and 3 use the gaussian gampling algorithm, they result in mapping zones with different smoothness levels. Whatsmore, all these sub-figures show that the Active-set algorithm finds more solutions than the SQP solutions.

We compared the mapping zones given by the particle swarm method and numerical continuation method (See Fig.4.2). We choose the particle swam algorithm using gaussian sampling initialisation $(\sigma = 0.5)$ to be compared, because it has the best result given by all three implemented cases (all these cases are using particle swarm method. One case uses the fixed initialisation method and other two cases use the

gaussian sampling method with different values of σ) . The second sub-figure presents the results obtained by solving the optimisation problem using the numerical continuation method, comparing the solution sets derived from the active-set and SQP solvers. The mapping zone obtained using the numerical continuation method is significantly smoother than the mapping zone obtained using the naive algorithm with gaussian sampling. However, the mapping zone given by the numerical continuation algorithm is much smaller than the particle swarm algorithm. Similar to the conclusion from the comparison between the fixed initialisation method and the gaussian sampling Method, for the numerical continuation algorithm, the Active-set solver also gives more solutions than the SQP solver, although, as shown in Table.4.1 that the SQP solver has a more expensive time cost. However, the Active-set Solver will break

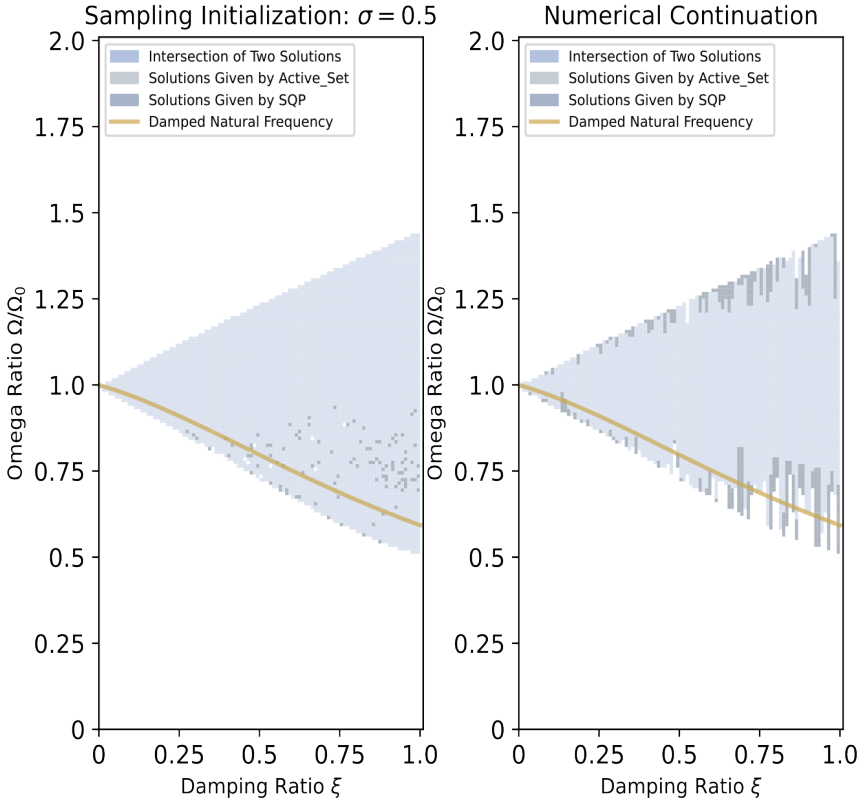

Figure 4.2: Mapping Zone: Particle Swarm vs. Numerical Continuation

down with extremely fine step-size, but the SQP Solver will always work. Thus, for the versatility of the whole numerical method, the SQP Solver is highly recommended.
In contrast to fixed initialization, the gaussian sampling initialization method for the particle swarm method is using 10 'guess' solutions that are better distributed across the $\mathbb{S}$ space. Given the search principle of the optimisation algorithm, which prioritises exploring local extreme points near initial 'guess' solutions and declares the optimi-

sation problem unfeasible if convergence is not achieved within a certain number of steps, the gaussian sampling initialization method enables the optimisation algorithm to identify more feasible solutions compared to the fixed initialisation method. However, the gaussian sampling method will also require more iterations for each potential solution. The worst-case scenario occurs when a tested potential solution which is inherently unfeasible, forcing the algorithm to evaluate all 'guess' solutions before getting the conclusion. For instance, if we employ 10 samples in the gaussian sampling method to test an unfeasible potential solution, the algorithm will expend 10 iterations before determining that this potential solution is unsuitable for our object optimisation problem. Consequently, this process can lead to a significant increase in computational time cost.

The superior efficiency of the numerical continuation method can be attributed to two primary factors: Firstly, based on the operational principles of the numerical continuation method, the optimization algorithm can more effectively locate potential solutions in the vicinity of existing 'guess' solutions during the search for feasible potential solutions. This significantly reduces the number of ineffective iterations, thereby shortening the algorithm's time-cost. Secondly, the numerical continuation method terminates once a complete solution branch is identified and will never explore beyond that boundary and test other solution branches automatically, which results in the identification of a narrower resonance band compared to the actual scenario. In a short word, the search window of the numerical continuation method is smaller, reducing computational time, which also means that the obtained solution domain is less comprehensive. In essence, while the numerical continuation method offers improved efficiency and reduced computational time, it may provide a more limited representation of the complete solution space compared to particle swarm methods.

To summarise all these properties of the algorithm working on a simple case, we offered a suggestion about how to popularise it to more complicated cases. To make up for the disadvantage that the numerical continuation method gives an incomplete mapping zone and sufficiently uses its advantage that it costs super less computation time and its capability of finding a nice smooth mapping zone, we choose to use the numerical continuation method to get a primary smooth mapping zone. Then, we use the particle swam method using gaussian sampling method to find the potential mapping zone that fulfils our need, which is missed by the numerical continuation method. In this way, we can try our best to ensure the final mapping zone's completeness and minimise the algorithm's whole-time cost. The related workflow is shown below.

Algorithm 4 Workflow with Composite method

Require: Initialization of parameters: Damping Ratio ξ, Natural Frequency ω_0

for Damping Ratio $\xi \rightarrow$ Defined Domain [0,$\cdots$] **do**

while Omega Ratio $\Theta = \frac{\omega}{\omega_0} \rightarrow$ Defined Domain [1,$\cdots$] **do**

Initialization: $\alpha = [a_1, 0, \cdots]$;

Optimization Solver(**SQP**);

Check the solution given by the solver

if Solution α^* fulfil the tolerance **then**

New Initialization for optimization Solver in next iteration: $\alpha = \alpha^*$;

else if Solution α^* doesn't fulfil the tolerance **then**

Initialization: Gaussian Sampling $\mathbf{A^0} = \beta_j$, β_j is j-th element in the Sample Set, $j = 1$;

Optimization Solver (**SQP**);

Check the solution given by the solver

if Solution α^* fulfil the tolerance **then**

Output the solution;

else if Solution α^* doesn't fulfil the tolerance **then**

j = j+1 (*!!Entrance of Gaussian Sampling!!*)

$\mathbf{A^0} = \beta_j$, β_j is j-th element in the Sample Set;

Optimization Solver;

Check the solution given by the solver

if Solution α^* fulfil the tolerance **then**

Output the solution;

Go to the 'Exit' Step

else if Solution α^* doesn't fulfil the tolerance **then**

Turn back to the 'Entrance of Gaussian Sampling' step

end if

end if

end if(*!!Exit!!*)

Update Omega Ratio with step width h: $\Theta_{\text{NEW}} = \frac{\omega}{\omega_0\,\text{NEW}} = \Theta_{\text{OLD}} + h = \frac{\omega}{\omega_0\,\text{Old}} + h$

end while

end for

Chapter 5

Extensions Implement to higher harmonics and nonlinear oscillators

We experiment with two different complicated cases to test the performance of the numerical algorithm: higher harmonic oscillator and a nonlinear oscillator. In both these cases, $x(t)$ is defined as a 6-term odd harmonic,

$$x(t) = a_1 \cos(\omega t) + a_2 \cos(3\omega t) + a_3 \cos(5\omega t) + a_4 \cos(7\omega t) + a_5 \cos(9\omega t) + a_6(11\omega t) \qquad (5.1)$$

which keeps similar geometry properties to the 3-term case, whose results have been shown in the above chapters. The equation of motion is given as Eq.2.7 in Chapter 2. The discretised parameters are similar to those in the 3-term odd harmonic case and the composite algorithm (See algorithm 4) is applied. We employ $\mathbf{A}^0 = [1, 0, 0, 0, 0, 0]$ as the initial guess solution for the numerical continuation method part of the whole optimisation algorithm. The numerical continuation method terminates upon discovering one solution branch, corresponding to identifying the 'inner' solution space. Subsequently, we utilise the boundary solution set obtained from the numerical continuation method as 'guess' solutions to initialise the second phase of the optimisation algorithm. This phase employs the particle swarm method to locate the 'outer' solution space of the optimisation problem. Ultimately, the 'inner' and 'outer' solution spaces are combined to form the complete solution domain. The band-type resonance mapping zones, work-loop and the power waveform are plotted to show the related results in Fig.5.1 (higher harmonic(linear) oscillator)and Fig.5.2 (nonlinear oscillator)

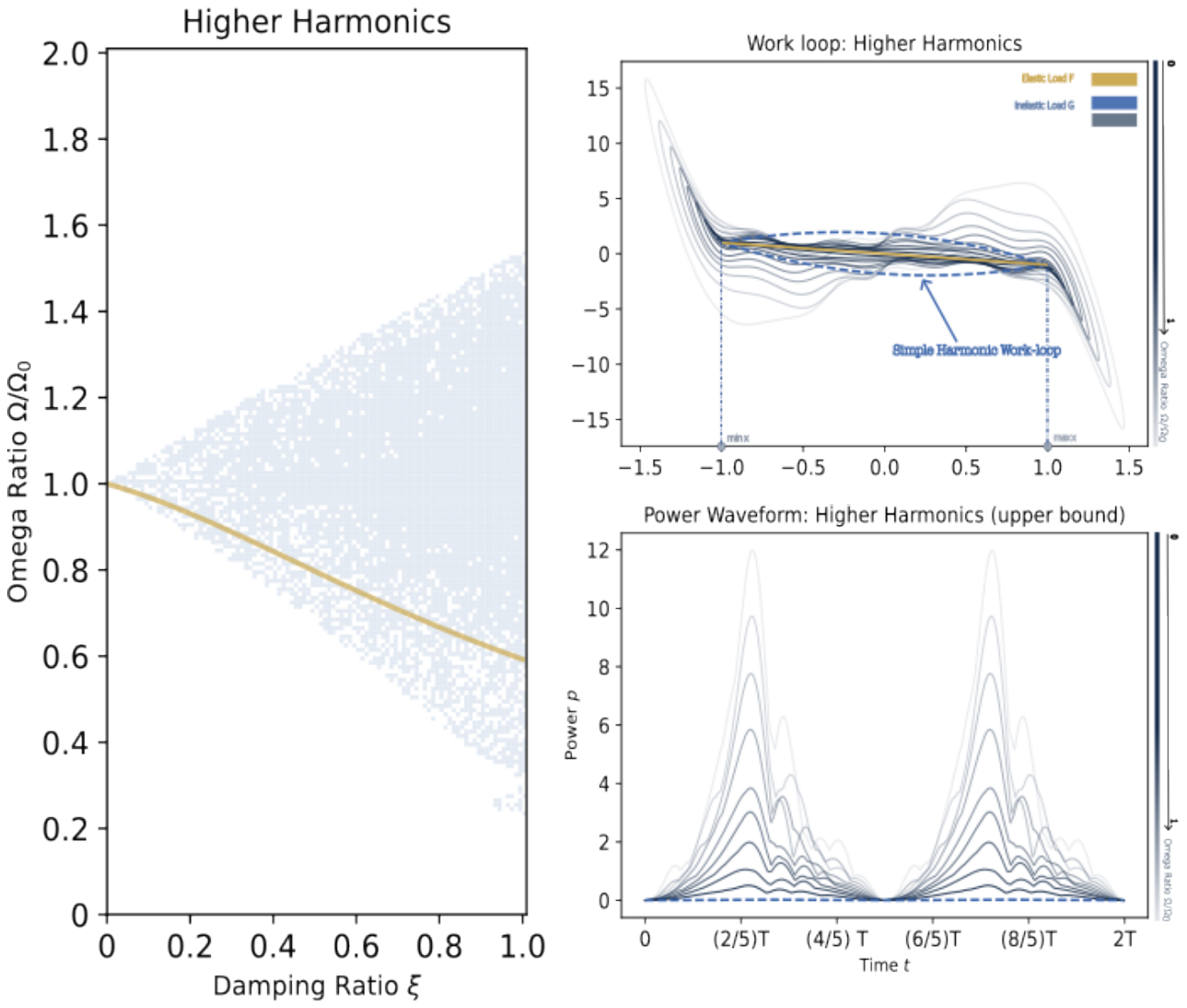

Figure 5.1: In this figure, we present the mapping zone, work-loop, and power waveform corresponding to the solutions of the higher harmonic oscillator system. In sub-figure (a), the mapping zone of the solution set is depicted in light blue, with the theoretical lower boundary provided by the analytical solution marked by a light yellow line. sub-figures (b) and (c) illustrate the work-loop and power waveform curves corresponding to 10 sample points taken from the higher boundary of the mapping zone. The parameter Ω/Ω_0 increases from 0 to 1, denoted as $\Omega/\Omega_0 \in [0, 1]$ corresponding to colours ranging from dark blue to light blue.

In the plots for the nonlinear oscillator, we have not provided reference lines for the analytical solution as was done in previous examples. This is because, to date, no research has successfully derived a theoretical solution for this problem in the context

of nonlinear oscillators. Nevertheless, our proposed numerical algorithm is still able to give reference mapping zone. The corresponding power waveforms demonstrate superior non-negativity properties, which can easily prove the accuracy and stability of the numerical algorithm.

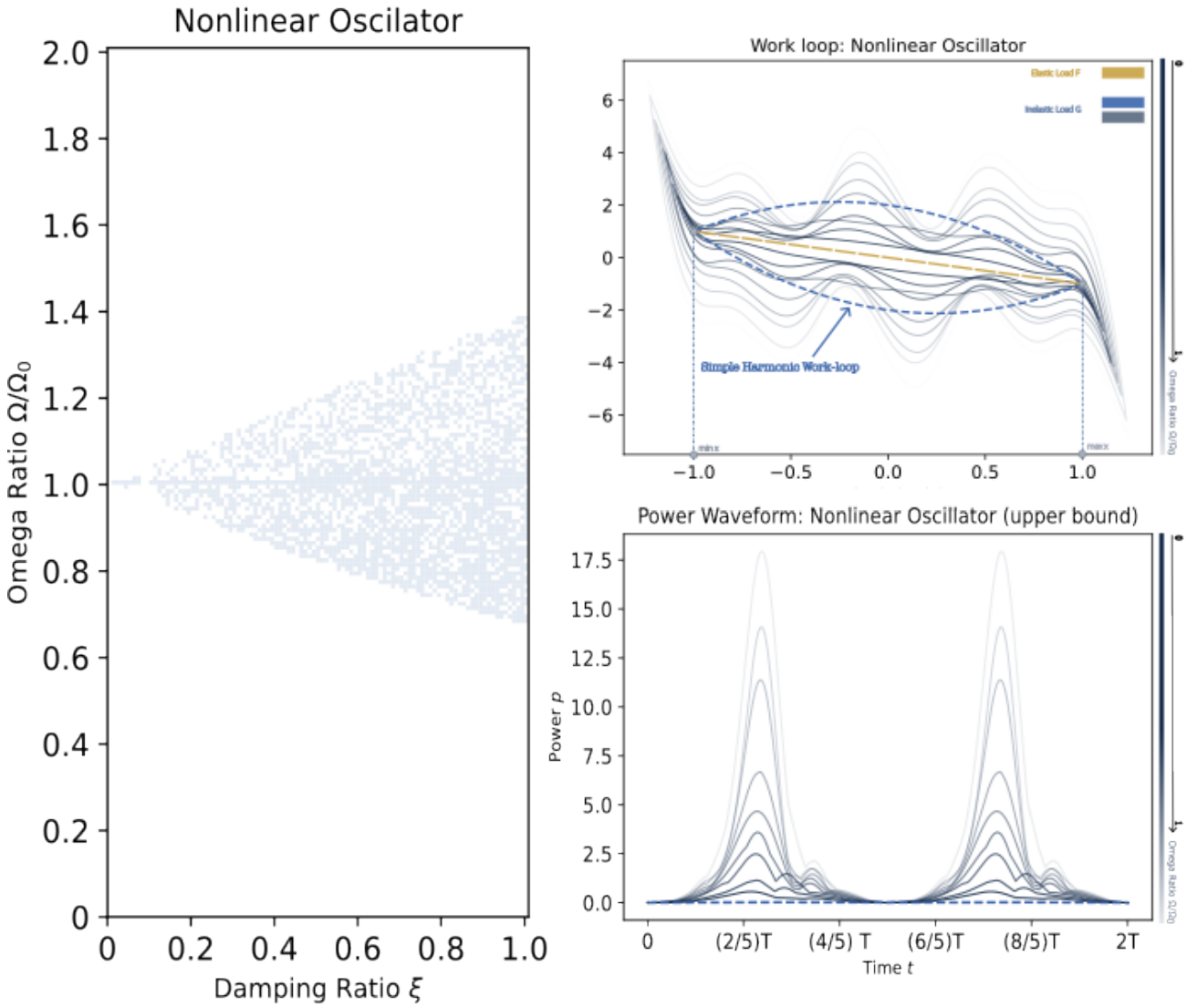

Figure 5.2: In this figure, we present the mapping zone, work-loop, and power waveform corresponding to the solutions of the nonlinear oscillator. In sub-figure (a), the mapping zone of the solution set is depicted in light blue. sub-figures (b) and (c) illustrate the work-loop and power waveform curves corresponding to 10 sample points taken from the higher boundary of the mapping zone. The parameter Ω/Ω_0 increases from 0 to 1, denoted as $\Omega/\Omega_0 \in [0, 1]$ corresponding to colours ranging from dark blue to light blue.

When dealing with higher harmonics and nonlinear oscillator systems, it is obvious to discover that the completeness of the mapping zone plotted by using the numerical continuation method is worse than what it provides for the simple case, particularly for the nonlinear harmonic oscillator. However, the particle swarm method still seems to work nicely.

For both cases, the work loop is now so ideal, as is mentioned in [28, 27], which can be proved by the plot of the power waveform that the power at the time around T will be significantly negative, which is quite different from the value of $\min p$ output by the optimisation algorithm.

Chapter 6

Conclusion

In this thesis, we formulated the problem of solving band-type resonance as an optimisation problem. To address this optimisation challenge, we employed particle swarm and numerical continuation methods to search for feasible solutions. For the particle swarm method, we explored two approaches: fixed initialisation and sampling initialisation. In the sampling initialization, we utilised a gaussian sampling method to initialise the optimisation algorithm, which resulted in a noticeably smoother solution space.
Comparing the particle swarm method with the numerical continuation method, we found that numerical continuation consumed less time and produced a smoother solution space relative to the Gaussian sampling method. The numerical continuation method ran into branch breaking points earlier as the complexity of the harmonic oscillator increased, but the solution space it discovered still had good smoothness characteristics.
To address the complicated problem, we adopted a hybrid approach:

- Using numerical continuation to calculate the central solution space.
- Employing the particle swarm method to search for potential solutions outside the breaking points

This strategy aimed to minimise code execution time while ensuring the smoothness and completeness of the solution space.
We note that our algorithm can be applied to more complex cases. A potential extension of this work would be to utilize alternative methods for the update step in the numerical continuation method. One rule that must be obeyed is that the choice of this update scheme follows different principles from classic numerical continuation methods. The updated estimation function, after parameter substitution, should have

similar extreme points to the original estimation function rather than zero points. Our novel method is relatively simple to implement, accurate, flexible, and computationally efficient. We anticipate that this technique will prove invaluable in problems requiring:

- Predictive understanding of band-type resonance mapping
- Solving energy-optimal solutions
- Analyzing aerodynamic behaviours in insect flight

The timely revival of these applications is relevant to a variety of current research in both biology and mechanics.

Bibliography

[1] E. L. Allgower and K. Georg, Numerical Continuation Methods, vol. 13 of Springer Series in Computational Mathematics, Springer Berlin Heidelberg.

[2] C. Bolsman, J. Goosen, and F. van Keulen, Design overview of a resonant wing actuation mechanism for application in flapping wing MAVs, 1, pp. 263–272. Publisher: SAGE Publications Sage UK: London, England.

[3] B. Bullard and A. Pastore, Through thick and thin: dual regulation of insect flight muscle and cardiac muscle compared, 40, pp. 99–110.

[4] T. Deora, N. Gundiah, and S. P. Sane, Mechanics of the thorax in flies, 220, pp. 1382–1395.

[5] W. B. Dickson, A. D. Straw, and M. H. Dickinson, Integrative Model of Drosophila Flight, AIAA Journal, 46 (2008), pp. 2150–2164.

[6] E. D. Dolan, NEOS server 4.0 administrative guide.

[7] C. Ellington, The aerodynamics of hovering insect flight. VI. Lift and power requirements, Philosophical Transactions of the Royal Society of London. B, Biological Sciences, 305 (1984), pp. 145–181.

[8] ——, The novel aerodynamics of insect flight: applications to micro-air vehicles, Journal of Experimental Biology, 202 (1999), pp. 3439–3448.

[9] A. P. Engelbrecht, Computational Intelligence: An Introduction, Wiley, 1 ed.

[10] A. G. Gad, Particle swarm optimization algorithm and its applications: A systematic review, 29, pp. 2531–2561.

[11] J. Gau, N. Gravish, and S. Sponberg, Indirect actuation reduces flight power requirements in *Manduca sexta* via elastic energy exchange, Journal of The Royal Society Interface, 16 (2019), p. 20190543.

[12] N. S. Ha, Q. T. Truong, N. S. Goo, and H. C. Park, Relationship between wingbeat frequency and resonant frequency of the wing in insects, 8, p. 046008.

[13] J. S. U. Hedlund, H. Lv, P. Lehmann, G. Hu, R. C. Anderson, and J. W. Chapman, Unraveling the Worlds Longest Non-stop Migration: The Indian Ocean Crossing of the Globe Skimmer Dragonfly, Frontiers in Ecology and Evolution, 9 (2021), p. 698128.

[14] A. Iserles, A First Course in the Numerical Analysis of Differential Equations, Cambridge University Press, 2 ed.

[15] H. Iwamoto, Structure, function and evolution of insect flight muscle, 7, pp. 21–28.

[16] M. A. Jankauski, Flapping at resonance: Measuring the frequency response of the hymenoptera thorax.

[17] R. K. Josephson, Comparative physiology of insect flight muscle, in Natures Versatile Engine: Insect Flight Muscle Inside and Out, Springer US, pp. 34–43. Series Title: Molecular Biology Intelligence Unit.

[18] R. K. Josephson, J. G. Malamud, and D. R. Stokes, Asynchronous muscle: A primer, 203, pp. 2713–2722.

[19] ——, Power output by an asynchronous flight muscle from a beetle, 203, pp. 2667–2689.

[20] Z. A. Khan and S. K. Agrawal, Design of flapping mechanisms based on transverse bending phenomena in insects, in Proceedings 2006 IEEE International Conference on Robotics and Automation, 2006. ICRA 2006., IEEE, pp. 2323–2328.

[21] K. J. Leitch, F. V. Ponce, W. B. Dickson, F. Van Breugel, and M. H. Dickinson, The long-distance flight behavior of *Drosophila* supports an agent-based model for wind-assisted dispersal in insects, Proceedings of the National Academy of Sciences, 118 (2021), p. e2013342118.

[22] J. Lynch, E. S. Wold, J. Gau, S. Sponberg, and N. Gravish, Energetic and control trade-offs in spring-wing systems.

[23] K. Y. Ma, S. M. Felton, and R. J. Wood, Design, fabrication, and modeling of the split actuator microrobotic bee, in 2012 IEEE/RSJ International Conference on Intelligent Robots and Systems, IEEE, pp. 1133–1140.

[24] R. McGill, N.-s. P. Hyun, and R. J. Wood, Frequency-modulated control for insect-scale flapping-wing vehicles, 7, pp. 12515–12522. Publisher: IEEE.

[25] A. Pons, Distribution-theoretic basis for hidden deltas in frequency-domain structural modelling, engrXiv, (2024).

[26] A. PONS AND T. BEATUS, Distinct forms of resonant optimality within insect indirect flight motors, Journal of The Royal Society Interface, 19 (2022), p. 20220080.

[27] ——, Elastic-bound conditions for energetically optimal elasticity and their implications for biomimetic propulsion systems, Nonlinear Dynamics, 108 (2022), pp. 2045–2074.

[28] ——, Band-type resonance: non-discrete energetically optimal resonant states, Nonlinear Dynamics, 111 (2023), pp. 1161–1192.

[29] A. PONS, I. PERL, O. BEN-DOV, R. MAYA, AND T. BEATUS, Solving the thoracic inverse problem in the fruit fly, Bioinspiration & Biomimetics, 18 (2023), p. 046002.

[30] S. P. SANE, The aerodynamics of insect flight, 206, pp. 4191–4208.

[31] K. WARFVINGE, M. KLEINHEERENBRINK, AND A. HEDENSTRM, The powerspeed relationship is U-shaped in two free-flying hawkmoths (*Manduca sexta*), Journal of The Royal Society Interface, 14 (2017), p. 20170372.

[32] T. WEIS-FOGH, Energetics of hovering flight in hummingbirds and in drosophila, 56, pp. 79–104. Publisher: The Company of Biologists Ltd.

[33] ——, Quick estimates of flight fitness in hovering animals, including novel mechanisms for lift production, 59, pp. 169–230. Publisher: The Company of Biologists Ltd.

[34] ——, A Rubber-Like Protein in Insect Cuticle, Journal of Experimental Biology, 37 (1960), pp. 889–907.

[35] E. S. WOLD, E. LIU, J. LYNCH, N. GRAVISH, AND S. SPONBERG, The weis-fogh number describes resonant performance tradeoffs in flapping insects, 64, pp. 632–643.

[36] R. J. WOOD, Design, fabrication, and analysis of a 3dof, 3cm flapping-wing MAV, in 2007 IEEE/RSJ international conference on intelligent robots and systems, IEEE, pp. 1576–1581.

[37] C. ZHANG, Numerical methods for mapping band-type resonance in insect flight, Dec. 2024.

[38] R. BIKOWSKI, S. A. ANSARI, AND K. KNOWLES, On mathematical modelling of insect flight dynamics in the context of micro air vehicles, 1, pp. R26–R37.

DEPARTMENT OF MATHEMATICAL SCIENCES
CHALMERS UNIVERSITY OF TECHNOLOGY
Gothenburg, Sweden 2024
www.chalmers.se

CHALMERS
UNIVERSITY OF TECHNOLOGY